
GeoAda: Efficiently Finetune Geometric Diffusion Models with Equivariant Adapters

Wanjia Zhao*, Jiaqi Han*, Siyi Gu, Mingjian Jiang, James Zou, Stefano Ermon
Department of Computer Science
Stanford University

Abstract

Geometric diffusion models have shown remarkable success in molecular dynamics and structure generation. However, efficiently fine-tuning them for downstream tasks with varying geometric controls remains underexplored. In this work, we propose an $SE(3)$ -equivariant adapter framework (GeoAda) that enables flexible and parameter-efficient fine-tuning for controlled generative tasks without modifying the original model architecture. GeoAda introduces a structured adapter design: control signals are first encoded through coupling operators, then processed by a trainable copy of selected pretrained model layers, and finally projected back via decoupling operators followed by an equivariant zero-initialized convolution. By fine-tuning only these lightweight adapter modules, GeoAda preserves the model’s geometric consistency while mitigating overfitting and catastrophic forgetting. We theoretically prove that the proposed adapters maintain $SE(3)$ -equivariance, ensuring that the geometric inductive biases of the pretrained diffusion model remain intact during adaptation. We demonstrate the wide applicability of GeoAda across diverse geometric control types, including frame control, global control, subgraph control, and a broad range of application domains such as particle dynamics, molecular dynamics, human motion prediction, and molecule generation. Empirical results show that GeoAda achieves state-of-the-art fine-tuning performance while preserving original task accuracy, whereas other baselines experience significant performance degradation due to overfitting and catastrophic forgetting.

1 Introduction

Diffusion models have emerged as powerful generative frameworks across a wide range of domains, including image synthesis [42, 36], robotics [34, 25], and molecular generation [21, 39, 37, 40]. In particular, geometric diffusion models [9] which incorporate spatial and symmetry-aware inductive biases have shown strong empirical performance in tasks such as particle dynamic prediction [13, 15, 26], molecular generation [3, 12] and protein-ligand binding structure prediction [7]. By modeling data in an equivariant network, these models are able to capture complex geometric relationships essential for physical and chemical systems.

However, despite their strong task-specific performance, existing geometric diffusion models lack the ability to generalize across tasks. In particular, it remains unclear how a model pretrained on one geometric generation task can be effectively adapted to a new task involving additional or different control signals. This limitation is especially pronounced in real-world molecular applications, where the available data across tasks are often highly imbalanced, and collecting labeled pretraining data for every new condition is costly and time-consuming. Without a mechanism for transfer, models must be retrained from scratch for each new task, which is inefficient and often leads to overfitting or loss of previously learned capabilities.

*Equal contribution. Correspondence to wanjiazh@cs.stanford.edu

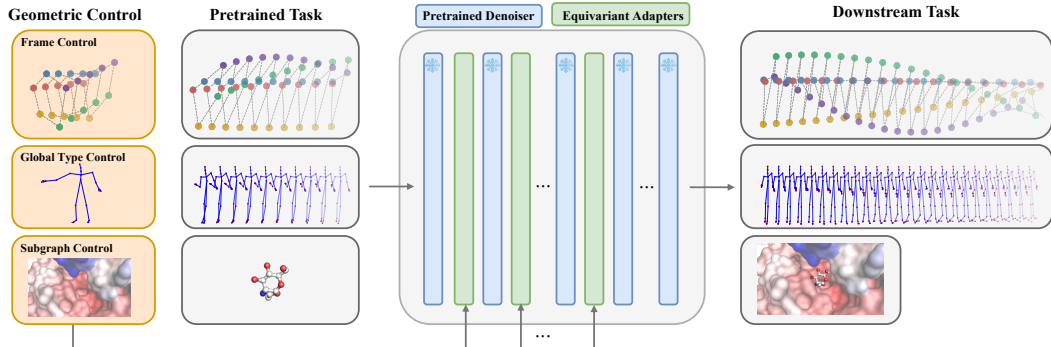


Figure 1: Overall framework of GeoAda. The model integrates diverse control signals, including frame, global type, and subgraph controls through lightweight equivariant adapters inserted into the frozen pretrained denoiser.

To this end, we propose a general and efficient framework (GeoAda) that enables the transfer of geometric diffusion models across diverse downstream tasks with minimal computational overhead. Inspired by the success of ControlNet [42] in conditional image generation, we introduce an equivariant adapter module that augments a pretrained geometric diffusion model with task-specific control capability. The Equivariant Adapter comprises two key components: 1) The equivariant adapter block that operates through a structured sequence—where control signals are encoded via coupling operators, processed by a trainable copy of selected pretrained model layers, and then decoded via decoupling operators. 2) Equivariant zero convolution, which acts as a safeguard for the original score by zeroing out the conditional contribution at initialization without blocking gradient updates. This design preserves the model’s $SE(3)$ -equivariance and allows modular, task-specific adaptation without altering the original model architecture. In addition to being lightweight and flexible, the adapter is parameter-efficient and implicitly regularized, thereby mitigating overfitting and preserving the performance of the pretrained model.

In summary, we make the following contributions: **1.** We propose an equivariant adapter framework (GeoAda) for geometric diffusion models that enables efficient task adaptation with minimal overhead. The adapter modules are lightweight and operate as plug-and-play components, allowing flexible conditioning on new control signals without architectural modifications to the pretrained model. **2.** GeoAda is parameter-efficient, introducing minimal overhead for downstream tasks compared to full fine-tuning, which updates the entire model and incurs substantial memory and computational costs. **3.** By freezing the pretrained model and introducing trainable adapters, GeoAda imposes implicit regularization, helping to mitigate overfitting and avoids catastrophic forgetting, thereby preserving performance on the pretraining task. **4.** We carefully design the adapter architecture to be $SE(3)$ -equivariant, ensuring that the adapted model retains the geometric inductive bias and the theoretical benefits of equivariant diffusion models, including $SE(3)$ -invariant marginal distributions during generation. **5.** We evaluate GeoAda across diverse geometric control types, including Frame Control, Global Type Control, Subgraph Control, and a wide range of application domains, such as particle dynamics, molecular dynamics, human motion prediction, and molecule generation. GeoAda consistently matches or outperforms full fine-tuning baselines on downstream task, while avoiding performance degradation on the original pretrain task—a common failure mode of naive tuning and prompt-base approaches.

2 Related Work

Geometric diffusion models. Recent diffusion models have been extended to 3D geometric data, with $SE(3)$ equivariance enabling physically consistent generation for tasks like molecular design and trajectory modeling. GeoDiff [40] pioneered this by learning stable molecular conformations through $SE(3)$ -invariant diffusion, while GeoLDM [39, 37] advanced scalability and controllability via structured latent spaces. GCDM [21] advanced large molecule generation by incorporating geometry-complete local frames and chirality-sensitive features into $SE(3)$ -equivariant networks. Moreover, diffusion augmented with geometric inductive bias has been explored in other domains such as 3D shape and scene generation [2] and robotics [34, 25]. Beyond static geometric modeling,

GeoTDM [9] and EquiJump [4] address dynamic 3D systems by introducing temporal attention mechanisms. However, existing geometric diffusion models lack cross-task generalization. Our framework enables efficient adaptation to new controls.

Finetuning for (geometric) graphs. Finetuning for geometric GNNs generally falls into two categories: prompt-based and adapter-based methods. Pioneering prompt-based approaches [32, 18] introduce virtual class-prototype nodes with learnable links for edge prediction pre-trained models, but lack generalizability to alternative pre-training strategies. Meanwhile, works like GPF [5] explore universal prompt-based tuning by adding shared learnable vectors to all node features in the graph. Adapter-based methods, exemplified by AdapterGNN [16], insert lightweight modules into GNN layers, achieving parameter-efficient adaptation across diverse graph domains.

Finetuning diffusion models. Recent research has proposed various strategies for fine-tuning diffusion models with improved efficiency, control [42], and alignment [35]. ELEGANT [33] formulates fine-tuning as an entropy-regularized control problem, directly optimizing entropy-enhanced rewards with neural SDEs. ControlNet [42] improves controllability by adding lightweight trainable branches to frozen diffusion backbones. Prompt Diffusion [36] enables training-free in-context learning for image-to-image tasks via example-based conditioning. However, fine-tuning diffusion models in geometric domains (e.g., particles, molecules) remains underexplored. GeoAda addresses this gap by enabling efficient and effective adaptation of diffusion models to geometric tasks.

3 Preliminaries

Geometric graphs and trajectories. We represent a *geometric graph* as $\mathcal{G} = (\mathcal{V}, \mathcal{E})$ where \mathcal{V} is the set of nodes and \mathcal{E} is the set of edges. In particular, each node i is equipped with certain node feature $\mathbf{h}_i \in \mathbb{R}^H$ representing its type or physical property, and the Euclidean coordinate $\mathbf{x}_i \in \mathbb{R}^3$ representing its spatial position. An edge exists between node i and j if they bear certain connectivity through, e.g., chemical bonds, or spatial proximity with a distance smaller than a cutoff. A *trajectory* is a generalization of geometric graph in the dynamical setting where the coordinates $\mathbf{x}_i^{[T]} \in \mathbb{R}^{3 \times T}$ are augmented with an additional temporal dimension, where T is the number of frames.

Geometric diffusion models. Geometric diffusion models are a family of generative models for capturing the distribution of geometric graphs and/or trajectories. Given an input data point \mathcal{G}_0 , they feature a forward noising process that gradually perturbs the clean data with a transition $q(\mathcal{G}_\tau | \mathcal{G}_0)$ where \mathcal{G}_τ converges to a tractable prior. A neural network $\epsilon_\theta(\mathcal{G}_\tau, \tau)$ (a.k.a. the denoiser) is learned to approximate the Stein score [31] through denoising score matching [29, 30, 11], which will be leveraged to derive the transition kernel $p_\theta(\mathcal{G}_{\tau-1} | \mathcal{G}_\tau)$ in the reverse process at sampling time. Notably, a core distinction of *geometric* diffusion models from others is that they enforce an SE(3)-invariant marginal, i.e.,

$$p_\theta(\mathcal{G}_0) = p_\theta(g \cdot \mathcal{G}_0), \quad \forall g \in \text{SE}(3), \quad (1)$$

by parameterizing the denoiser ϵ_θ with an SE(3)-equivariant architecture [12, 40], i.e.,

$$\epsilon_\theta(g \cdot \mathcal{G}_\tau, \tau) = g \cdot \epsilon_\theta(\mathcal{G}_\tau, \tau), \quad (2)$$

where SE(3) is the Special Euclidean group consisting of all rotations and translations in 3D.

4 Method

In this section, we detail our approach, equivariant adapter for geometric diffusion models. We first specify three types of controls in § 4.1 that are ubiquitously enforced to geometric diffusion models in various downstream tasks. In § 4.2, we propose an architecture-agnostic and principled recipe for encoding such controls that seamlessly enables finetuning on the pretrained denoiser. In § 4.3, we present our design of GeoAda, a plug-in-and-play adapter module tuned for each downstream task that unlocks transferability.

4.1 Geometric Controls for Geometric Diffusion Models

In this work, we aim to transfer the generation capability of pretrained geometric diffusion models to downstream tasks where additional *geometric controls* present. Specifically, we are concerned with

three different types of geometric controls, namely global type control \mathbb{C}_G , subgraph control \mathbb{C}_S , and frame control \mathbb{C}_F , as detailed below.

Global type control. Each global type control $\tilde{c} \in \mathbb{C}_G$ is a vector in \mathbb{R}^K describing certain global signal enforced on the geometric graph, such as an encoding of the class label, some quantum chemical property of the molecule [12], or even the embedding of some text prompt [20].

Subgraph control. Each subgraph control $\tilde{G} = (\tilde{\mathcal{V}}, \tilde{\mathcal{E}}) \in \mathbb{C}_S$ is represented as a geometric graph with the set of nodes $\tilde{\mathcal{V}}$ and edges $\tilde{\mathcal{E}}$. Subgraph control widely exists in scenarios where generating a geometric graph conditioned on another fixed subgraph is of interest. For example, in the task of pocket-conditioned ligand generation [7], the protein pocket is viewed as the fixed subgraph \tilde{G} while a geometric diffusion model is learned to generate the ligand, conditioned on \tilde{G} .

Frame control. Each frame control in \mathbb{C}_F takes the form of a sequence of additional \tilde{T} frames, namely $\tilde{\mathbf{x}}_i^{[\tilde{T}]} \in \mathbb{R}^{3 \times \tilde{T}}$ for each node i . Frame controls are enforced in cases when, *e.g.*, a trajectory has been partially observed and the model is expected to generate the future or missing frames conditioned on the observed frames.

4.2 Encoding Geometric Controls

In this subsection, we propose a simple yet effective approach for incorporating the geometric controls into the denoiser *without* modifying its architecture. Such feature is critical since it enables us to initialize the denoiser fully with the pretrained checkpoint when performing finetuning on downstream tasks, thus significantly alleviating optimization overheads and potential inconsistencies in the parameter space. More importantly, our design is also guaranteed to preserve the equivariance of the denoiser, a fundamental principle that leads to the success of geometric diffusion models.

In form, given the denoiser $\epsilon_\theta(\mathcal{G}_\tau, \tau)$, we seek to devise $\epsilon_\theta(\mathcal{G}_\tau, \tau, \mathcal{C})$ where $\mathcal{C} \in \mathbb{C}_G \cup \mathbb{C}_S \cup \mathbb{C}_F$ is any of the control we specified in § 4.1. Our core observation lies in that each type of the control can be encoded through certain coupling operator $\mathbf{f}(\mathcal{G}_\tau, \mathcal{C})$ of the input noised graph \mathcal{G}_τ and control \mathcal{C} , and a corresponding decoupling operator \mathbf{g} that extracts the scores on the nodes and frames in \mathcal{G}_τ from the output of ϵ_θ . We introduce our design of \mathbf{f} and \mathbf{g} with respect to different controls as follows.

Global type control. For global type control $\mathcal{C}_G := \tilde{c} \in \mathbb{R}^K$, we design \mathbf{f} as a node-wise addition of the input node feature and a linear transformation of the control \tilde{c} , *i.e.*, $\mathcal{V}', \mathcal{E}' = \mathbf{f}(\mathcal{V}, \mathcal{E}, \mathcal{C})$, where

$$\mathcal{V}' = (\{\mathbf{x}_i\}, \{\mathbf{h}_i + \sigma(\tilde{c})\}), \quad \mathcal{E}' = \mathcal{E}, \quad (3)$$

where $\sigma : \mathbb{R}^K \mapsto \mathbb{R}^H$ is an MLP that lifts the control signal to the node feature space. We use identity function as the decoupling operator \mathbf{g} .

Subgraph control. For subgraph control $\mathcal{C}_S := \tilde{G}$, the coupling operator \mathbf{f} is realized by computing the supergraph of the input \mathcal{G} and the control \tilde{G} , *i.e.*, $\mathcal{V}', \mathcal{E}' = \mathbf{f}(\mathcal{V}, \mathcal{E}, \mathcal{C})$, where

$$\mathcal{V}' = \mathcal{V} \cup \tilde{\mathcal{V}}, \quad \mathcal{E}' = \mathcal{E} \cup \tilde{\mathcal{E}}. \quad (4)$$

The decoupling operator \mathbf{g} is implemented by extracting the features of subgraph that corresponds to the nodes in the input graph \mathcal{G} from the output of ϵ_θ .

Frame control. For frame control $\mathcal{C}_F := \{\tilde{\mathbf{x}}_i^{[\tilde{T}]}\}$, we implement \mathbf{f} as a concatenation of the input frames and the frame control, *i.e.*, $\mathcal{V}', \mathcal{E}' = \mathbf{f}(\mathcal{V}, \mathcal{E}, \mathcal{C})$, where

$$\mathcal{V}' = (\{\text{concat}(\mathbf{x}_i^{[T]}, \tilde{\mathbf{x}}_i^{[\tilde{T}]})\}, \{\mathbf{h}_i\}), \quad \mathcal{E}' = \mathcal{E}, \quad (5)$$

and \mathbf{g} performs the reverse operation by discarding the frames corresponding to $[\tilde{T}]$ from the output of ϵ_θ .

Proposition 4.1 (Equivariance of control encoding). *If the denoiser ϵ_θ is $SE(3)$ -equivariant, the composition $\mathbf{g} \circ \epsilon_\theta \circ \mathbf{f}$ is also $SE(3)$ -equivariant, for all controls $\mathcal{C} \in \mathbb{C}$.*

4.3 Equivariant Adapters

With the control encoding in § 4.2, a straightforward approach to leverage a pretrained diffusion model on downstream tasks is to perform supervised finetuning (SFT). However, SFT usually induces suboptimal empirical performance, since **1.** SFT is parameter-inefficient since each gradient update is conducted on all parameters of the pretrained model; **2.** the full-parameter finetuning is prone to overfitting with limited amount of finetuning data; and **3.** the model finetuned after SFT loses performance guarantee on the original task, a phenomenon widely acknowledged as catastrophic forgetting.

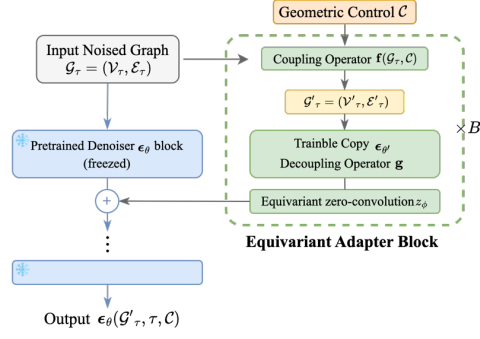


Figure 2: Overall Framework

To address these challenges, we draw inspiration from the successful application of adapters on image diffusion models, *e.g.*, ControlNet [43], to devise a diffusion adapter for geometric diffusion models. Our approach, dubbed equivariant adapter, is a lightweight tunable module plugged-in on top of the pretrained model, which is optimized for each downstream task.

The equivariant adapter block. In detail, each equivariant adapter block is responsible for processing the control signal and fusing it into the score produced by the pretrained model, whose parameters are always frozen at finetuning stage. Each adapter block consists of, in a sequential manner, the coupling operator \mathbf{f} , a *trainable copy* of the corresponding layers in pretrained model $\epsilon_{\theta'}$, the decoupling operator \mathbf{g} , followed by an equivariant *zero-convolution* layer.

Specifically, the composition $\mathbf{g} \circ \epsilon_{\theta'} \circ \mathbf{f}$, as depicted in § 4.2, functions altogether as a conditional score network $\epsilon_{\theta'}(\mathcal{G}_\tau, \tau, \mathcal{C})$ that captures the bias of the control signal on the original score $\epsilon_\theta(\mathcal{G}_\tau, \tau)$ while ensuring the SE(3)-equivariance of the conditional score. Moreover, $\epsilon_{\theta'}$ can be initialized as a subset of the layers in the pretrained model ϵ_θ , thus reducing the total number of tunable parameters compared with SFT. While the selection strategy can be arbitrary, empirically we have found that selecting the first layer for every K consecutive layers from the pretrained model performs more favorably compared with naive choices such as the initial or last several layers, under the same parameter budget (*c.f.*, § 5.4).

Equivariant zero-convolution. While the equivariant adapter block offers a parameter-efficient way of modeling the conditional score, its non-zero initialization introduces additional noise when it is added to the original score ϵ_θ , leading to instability at the beginning of the finetuning stage. To alleviate such issue, we borrow insight from the *zero-convolution* module proposed in [42] that acts as a safeguard of the original score by zeroing out the conditional score at initialization without blocking the gradient update.

For any $(\{\mathbf{x}_i\}, \{\mathbf{h}_i\})$, equivariant zero-convolution is given by

$$z_\phi(\{\mathbf{x}_i\}, \{\mathbf{h}_i\}) = (\{\phi_{\mathbf{x}} \cdot (\mathbf{x}_i - \bar{\mathbf{x}})\}, \{\phi_{\mathbf{h}} \cdot \mathbf{h}_i\}), \quad (6)$$

where $\bar{\mathbf{x}} = \frac{1}{N} \sum_{i=1}^N \mathbf{x}_i$ is the center-of-mass of the input graph, and $\phi_{\mathbf{x}} \in \mathbb{R}$, $\phi_{\mathbf{h}} \in \mathbb{R}^H$ are learnable parameters initialized all as zero. By such design, we guarantee that each equivariant adapter block, when equipped with equivariant zero-convolution, yields a rotation-equivariant and translation-invariant output, hence the SE(3)-equivariance of the conditional score after adding the output to the original score. Furthermore, the output of equivariant adapter block will always be zero at initialization, which does not affect the original score, thus enabling smooth and noiseless optimization when tuning the adapter.

4.4 Overall Framework

The overall framework of our adapter is depicted in Fig. 2. In general, our adapter is comprised of B equivariant adapter blocks, where each block is a sequential stack of the coupling operator \mathbf{f} , the trainable copy of one layer of the denoiser, the decoupling operator \mathbf{g} , and a zero-convolution module. At finetuning stage, all parameters in the original denoiser are frozen while the trainable copies and coefficients in zero-convolution are updated through gradient coming from minimizing the denoising

loss

$$\mathcal{L}_{\text{finetune}}(\theta', \phi) = \mathbb{E}_{\epsilon \sim \mathcal{N}(\mathbf{0}, \mathbf{I}), (\mathcal{G}, \mathcal{C}) \sim \mathbb{D}, \tau \in \text{Unif}(0, T)} \|\epsilon_{\theta}(\mathcal{G}_{\tau}, \tau) + \mathbf{s}_{\theta', \phi}(\mathcal{G}_{\tau}, \tau, \mathcal{C}) - \epsilon\|_2^2, \quad (7)$$

where \mathbb{D} is the downstream dataset, \mathcal{G}_{τ} is the noised graph drawn from $q(\mathcal{G}_{\tau}|\mathcal{G}_0)$, and $\mathbf{s}_{\theta', \phi}$ refers to our proposed equivariant diffusion adapter. At inference time, we use $\epsilon_{\theta}(\mathcal{G}_{\tau}, \tau) + \mathbf{s}_{\theta', \phi}(\mathcal{G}_{\tau}, \tau, \mathcal{C})$ as the conditional score when computing the reverse transition kernel $p(\mathcal{G}_{\tau-1}|\mathcal{G}_{\tau}, \mathcal{C})$.

Our GeoAda offers several key advantages over standard supervised fine-tuning (SFT): **1.** The adapter modules are lightweight and operate as plug-and-play components, allowing flexible conditioning on new control signals without architectural modifications to the pretrained model. **2.** Parameter-efficient, as only a subset of trainable adapter modules are introduced. **3.** By freezing the Pretrained model and only optimizing lightweight adapters, the method imposes implicit regularization, helping to prevent overfitting. **4.** Through the careful design of SE(3)-equivariant adapter blocks and zero convolutions, GeoAda guarantees equivariance throughout the tuning process, thereby retaining the theoretical benefits of geometric diffusion models.

5 Experiment

We evaluate GeoAda across three categories of additional fine-tuning controls: (1) Frame control during dynamic prediction (§ 5.1), (2) Global type control in human motion prediction (§ 5.2), and (3) Subgraph control in molecule generation (§ 5.3). We also performed ablation studies on core design choices and present some observations in § 5.4.

Baselines. We compare with three types of baselines: (1) *Fine-tuning* methods, including **Full FT**, which fine-tunes the entire model, and **PARTIAL- k** [10, 14, 43], which updates only the last k layers of the pre-trained model; (2) *Prompt-based* methods, including **GPF**, **GPF-plus** [5], which both inject learnable prompt features into the input space. And **Prompt-Template** maps new inputs to pre-training-style inputs using manually designed graph templates, specifically for the conditional case. (3) *Head-only* tuning methods, where **MLP- k** freezes the pre-trained model and uses a k -layer MLP as the prediction head. To preserve equivariance, we replace the MLP with an EGTN block in our implementation. More details can be found in App. 8.2.

Implementation. The input data are processed as geometric graphs. We use 3 GeoAda blocks with hidden dimension of 128. We use $\mathcal{T} = 1000$ and linear noise schedule [11]. More details in App. 8.1.

5.1 Frame Control

Task setup. For pre-training, we use the first 10 frames as the condition and train the model to predict the trajectory over the following 20 frames. In the downstream task, we adopt a different setup where the model observes 15 conditional frames and predicts the next 20 frames. We evaluate all models on both the original task and the new task to assess their generalization and adaptability across different settings.

Metrics. We employ Average Discrepancy Error (ADE) and Final Discrepancy Error (FDE), which are widely adopted for trajectory forecasting [41, 38], given by $\text{ADE}(\mathbf{x}^{[T]}, \mathbf{y}^{[T]}) = \frac{1}{TN} \sum_{t=0}^{T-1} \sum_{i=0}^{N-1} \|\mathbf{x}_i^{(t)} - \mathbf{y}_i^{(t)}\|_2$, and $\text{FDE}(\mathbf{x}^{[T]}, \mathbf{y}^{[T]}) = \frac{1}{N} \sum_{i=0}^{N-1} \|\mathbf{x}_i^{(T-1)} - \mathbf{y}_i^{(T-1)}\|_2$. For probabilistic models, we report average ADE and FDE derived from $K = 5$ samples.

5.1.1 Particle Dynamic

Experimental Setup. We adopt the CHARGED PARTICLES dataset [15, 26] for particle dynamics simulation. In this dataset, $N = 5$ particles with randomly assigned charges of either +1 or -1 interact via Coulomb forces, resulting in complex, non-linear trajectories. We use 3000 trajectories for training, 2000 for validation, and 2000 for testing. We explore two settings: (1) Conditional trajectory generation: we use the first 10 frames of each trajectory as input to predict the subsequent 20 frames during pretraining, and 15 frames as input during finetuning to predict the next 20 frames. (2) Unconditional trajectory generation: we generate trajectories of length 20 from scratch during pretraining. During finetuning, we condition on the first 10 frames and predict the next 20 frames.

Table 1: Comparisons on CHARGED PARTICLES dataset.(all results reported by $\times 10^{-1}$).(\uparrow) / (\downarrow) denotes whether a larger / smaller number is preferred.

Setting Task Metric	Uncondition					Condition			
	FT		Pretrain			FT		Pretrain	
	ADE(\downarrow)	FDE(\downarrow)	Marg(\downarrow)	Class(\uparrow)	Pred(\downarrow)	ADE(\downarrow)	FDE(\downarrow)	ADE(\downarrow)	FDE(\downarrow)
Pretrain	nan	nan	0.079 \pm 0.000	5.149 \pm 0.285	0.109 \pm 0.004	11.826 \pm 0.133	20.395 \pm 0.249	1.177 \pm 0.018	2.815 \pm 0.037
Full FT	1.093 \pm 0.014	2.676 \pm 0.024	1.025 \pm 0.000	nan	nan	1.106 \pm 0.007	2.590 \pm 0.040	5.998 \pm 0.041	11.75 \pm 0.107
Prompt-Tem	-	-	-	-	-	1.723 \pm 0.014	3.703 \pm 0.061	nan	nan
PARTIAL- k [10]	1.685 \pm 0.006	3.594 \pm 0.040	1.016 \pm 0.000	nan	nan	1.409 \pm 0.009	3.330 \pm 0.042	9.325 \pm 0.064	11.94 \pm 0.149
MLP- k	6.258 \pm 0.947	9.111 \pm 2.628	1.015 \pm 0.000	0.00 \pm 0.000	5.740 \pm 2.914	1.503 \pm 0.016	3.338 \pm 0.039	3924	3950
GPF [5]	1.643 \pm 0.014	3.671 \pm 0.029	1.027 \pm 0.000	nan	nan	1.575 \pm 0.017	3.390 \pm 0.050	nan	nan
GPF-plus [5]	1.596 \pm 0.011	3.574 \pm 0.024	1.023 \pm 0.000	nan	nan	1.648 \pm 0.009	3.670 \pm 0.030	nan	nan
GeoAda	1.119 \pm 0.019	2.669 \pm 0.022	0.079 \pm 0.000	5.134 \pm 0.247	0.111 \pm 0.006	1.105 \pm 0.012	2.621 \pm 0.033	1.175 \pm 0.033	2.806 \pm 0.033

Results. We present the results in Table 1, with the following observations. Under both the unconditional and conditional trajectory generation settings, GeoAda achieves comparable or better performance than Full FT on the downstream task (conditioning on the first 10 frames to predict the next 20), while only tuning half the number of parameters. Furthermore, it consistently outperforms other fine-tuning and prompt-based baselines, achieving 35.69% improvement on ADE and 21.29% on FDE. On the original pretraining task, all baselines exhibit substantial performance degradation, with some failing to generate valid diffusion samples, indicating that these methods suffer from overfitting and catastrophic forgetting due to excessive adaptation to the downstream task."In contrast, by leveraging equivariant zero convolutions, GeoAda retains the pretrained model’s performance.

5.1.2 Molecular Dynamics

Experimental setup. We employ the MD17 [3] dataset, which contains the DFT-simulated molecular dynamics (MD) trajectories of 8 small molecules, with the number of atoms for each molecule ranging from 9 (Ethanol and Malonaldehyde) to 21 (Aspirin). For each molecule, we construct a training set of 5000 trajectories, and 1000/1000 for validation and testing, uniformly sampled along the time dimension. Different from [38], we explicitly involve the hydrogen atoms which contribute most to the vibrations of the trajectory, leading to a more challenging task. The node feature is the one-hot encodings of atomic number [27] and edges are connected between atoms within three hops measured in atomic bonds [28].

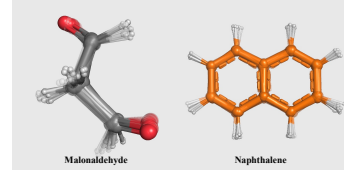


Figure 3: Visualization of MD17

Results. As shown in Table 2, GeoAda achieves state-of-the-art performance across all five molecular systems in the MD17 dataset, indicating strong transferability in geometric diffusion models. In downstream fine-tuning tasks, the method consistently matches or exceeds the performance of full fine-tuning and outperforms other prior methods by an average of 18.94% in ADE and 18.22% in FDE. Importantly, when returning to the original pretraining task, it retains performance comparable to the pretrained model, while both fine-tuning and prompt-based methods exhibit significant degradation or collapse due to overfitting. More experiment results on Malonaldehyde and Naphthalene in App. 9.1.

Table 2: Comparisons for Molecular Dynamics prediction on MD17 dataset (all results reported by $\times 10^{-1}$). The best results are highlighted in bold. Results averaged over 5 runs

Scenarios Task Metric	Aspirin				Benzene				Ethanol			
	FT		Pretrain		FT		Pretrain		FT		Pretrain	
	ADE	FDE	ADE	FDE	ADE	FDE	ADE	FDE	ADE	FDE	ADE	FDE
Pretrain	3.782 \pm 0.010	7.345 \pm 0.016	1.062 \pm 0.002	1.857 \pm 0.013	0.603 \pm 0.000	1.325 \pm 0.008	0.241 \pm 0.000	0.393 \pm 0.002	3.263 \pm 0.010	4.357 \pm 0.014	0.999 \pm 0.009	1.856 \pm 0.032
Full FT	0.929 \pm 0.002	1.602 \pm 0.005	1.323 \pm 0.003	2.280 \pm 0.016	0.217 \pm 0.001	0.360 \pm 0.002	nan	nan	0.997 \pm 0.007	1.906 \pm 0.002	inf	inf
PARTIAL- k [10]	1.071 \pm 0.003	1.875 \pm 0.009	1.439 \pm 0.003	2.407 \pm 0.007	0.249 \pm 0.005	0.407 \pm 0.003	0.318 \pm 0.110/nan	0.491 \pm 0.001/nan	1.288 \pm 0.008	2.161 \pm 0.018	6.502 \pm 4.574	4.636 \pm 2.423
MLP- k	1.132 \pm 0.004	1.921 \pm 0.004	1.579 \pm 0.005	2.641 \pm 0.007	0.248 \pm 0.012	0.412 \pm 0.004	nan	nan	1.301 \pm 0.001	2.275 \pm 0.021	2.228 \pm 0.004	2.716 \pm 0.022
Prompt-Tem	1.197 \pm 0.008	2.014 \pm 0.030	1.571 \pm 0.010	2.668 \pm 0.021	0.241 \pm 0.012	0.409 \pm 0.021	nan	nan	1.207 \pm 0.018	2.194 \pm 0.081	nan	nan
GPF [5]	1.130 \pm 0.006	1.909 \pm 0.024	3.260 \pm 0.015/inf	4.272 \pm 0.025/inf	0.246 \pm 0.001	0.415 \pm 0.004	nan	nan	1.239 \pm 0.023	2.233 \pm 0.059	2.420 \pm 0.156	3.519 \pm 0.056
GPF-plus [5]	1.014 \pm 0.006	1.962 \pm 0.021	2.243 \pm 0.009	3.349 \pm 0.018	0.234 \pm 0.010	0.331 \pm 0.057	1.118 \pm 0.006	1.083 \pm 0.010	1.137 \pm 0.025	2.048 \pm 0.046	3.240 \pm 0.081/inf	4.074 \pm 0.171/inf
GeoAda	0.891 \pm 0.003	1.533 \pm 0.008	1.060 \pm 0.003	1.852 \pm 0.012	0.191 \pm 0.000	0.319 \pm 0.002	0.240 \pm 0.002	0.394 \pm 0.005	0.905 \pm 0.007	1.745 \pm 0.010	0.995 \pm 0.005	1.867 \pm 0.019

5.2 Global Type Control

Experimental setup. The CMU Mocap dataset is a commonly used dataset for human pose prediction, which includes 8 action categories. A single pose has 38 body joints in the original dataset, among which we choose 25 joints. For pre-training, we construct a dataset by combining the

three most frequent actions: directing traffic, washing windows, and giving basketball signals. The remaining five actions are used as the downstream task fine-tuning dataset.

Results We report short-term and long-term motion prediction results on the CMU Mocap dataset in Tables 3 and 4. More results on jumping and soccer scenarios are in App. 9.2. GeoAda consistently achieves state-of-the-art performance across all action categories and time horizons. In this setting, the pretraining dataset is significantly larger than the downstream task dataset (30k vs. 245–1345 datapoints). As a result, naïve fine-tuning and prompt-based methods are highly prone to overfitting to the limited downstream training data, leading to notably degraded performance. Moreover, they are more likely to fail to generate valid samples on the original pretraining task, indicating a severe loss of pretrained knowledge and catastrophic forgetting. In contrast, GeoAda benefits from the implicit regularization effect of the adapter, which mitigates overfitting and preserves the performance of the pretrained model.

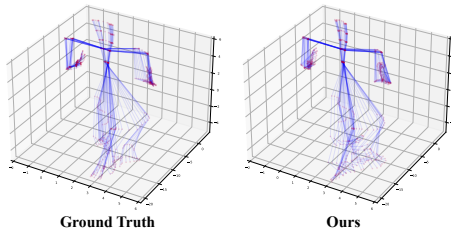


Figure 4: Visualization of Running trajectory

Table 3: Comparisons for short-term prediction on 5 action categories of the CMU Mocap dataset. The best results are highlighted in bold. Results averaged over 5 runs (std in App. 9.2).

scenarios	running				pretrain				walking				pretrain				basketball				pretrain			
	80	160	320	400	80	160	320	400	80	160	320	400	80	160	320	400	80	160	320	400	80	160	320	400
Pretrain	28.74	57.99	126.20	159.37	7.941	16.84	39.91	52.45	15.49	30.66	68.71	89.23	7.941	16.84	39.91	52.45	17.92	35.89	78.48	101.12	7.941	16.84	39.91	52.45
Full FT	20.34	35.26	60.58	70.20	nan	nan	nan	nan	10.01	15.12	23.98	28.49	nan	nan	nan	nan	16.95	30.33	58.28	71.93	nan	nan	nan	nan
PARTIAL- k [10]	20.47	36.04	68.15	82.59	nan	nan	nan	nan	10.47	16.97	30.97	37.69	17.26	31.75	66.29	84.27	17.54	32.03	62.96	78.95	nan	nan	nan	nan
MLP- k	23.35	44.44	84.27	101.42	nan	nan	nan	nan	10.86	18.74	35.78	44.86	nan	nan	nan	nan	17.60	34.76	72.90	86.34	nan	nan	nan	nan
GPF [5]	18.48	31.94	58.80	73.56	21.38	35.44	65.23	79.55	10.79	16.79	28.32	33.48	22.04	37.10	71.24	88.23	18.48	31.94	58.80	73.56	21.38	35.44	65.23	79.55
GPF-plus [5]	19.11	31.93	49.85	56.67	nan	nan	nan	nan	10.17	16.23	26.29	31.54	nan	nan	nan	nan	17.17	31.86	58.48	72.71	nan	nan	nan	nan
GeoAda	18.70	33.56	50.26	55.54	7.972	16.91	40.06	52.61	8.92	13.82	22.99	26.68	7.932	16.90	38.96	52.54	16.85	29.71	57.59	71.19	7.898	16.79	39.70	52.50

Table 4: Comparisons for long-term prediction on 5 action categories of the CMU Mocap dataset. The best results are highlighted in bold. Results averaged over 5 runs (std in App. 9.2).

scenarios	running		pretrain		walking		pretrain		basketball		pretrain	
	560	1000	560	1000	560	1000	560	1000	560	1000	560	1000
Pretrain	219.16	314.85	77.06	130.51	129.43	212.94	77.06	130.51	143.49	223.99	77.06	130.51
Full FT	85.14	97.02	nan	nan	36.92	52.58	nan	nan	94.59	132.34	nan	nan
PARTIAL- k [10]	102.85	108.47	nan	nan	51.36	84.72	118.82	182.88	106.84	146.27	nan	nan
MLP- k	127.67	131.59	nan	nan	62.97	102.34	nan	nan	107.30	149.58	nan	nan
GPF [5]	61.92	71.42	nan	nan	42.37	52.24	119.43	171.74	97.16	128.29	nan	nan
GPF-plus [5]	63.56	71.60	nan	nan	41.31	56.47	nan	nan	104.54	130.76	104.51	155.02
GeoAda	60.88	70.22	77.22	130.17	34.52	50.49	78.12	129.97	91.03	120.35	76.94	129.81

5.3 Subgraph Control

Experimental setup. We adopt the QM9 [24] and GEOM-Drugs [1] dataset for pretraining a model for molecule generation, use and the CrossDocked2020 dataset [6] for finetuning protein-ligand pair generation. QM9 [24] contains 130k small molecules with atom types (H, C, N, O, F). GEOM-Drugs [1] is a large-scale dataset of 430k molecular conformers with heavy atoms, and we keep the lowest energy conformation for each molecule. Following the common setup for CrossDocked2020 [8], we obtain 100k complexes for training and 100 novel complexes for testing. Since CrossDocked2020 has different atom type configuration from QM9 and GEOM-Drugs, we limit the atom type to (H, C, N, O, F, P, S, Cl). Following [8], proteins and ligands are expressed as 3D atom coordinates and one-hot vectors containing the atom types.

Implementation. Following prior work [8], we use the Adam optimizer with a learning rate of 0.001 and β values of (0.95, 0.999). Batch size is set to 4 and gradient clipping set to 8. To balance the atom type and position losses, we scale the atom type loss by a factor of $\lambda = 100$.

Results. We evaluate molecular properties and molecular structures of the proposed model and baselines on target-aware molecule generation in Table 5, 6, and 7. Baseline models are trained on CrossDocked2020 under explicit protein conditioning. GeoAda matches, and in multiple cases surpasses the strongest baselines on all metrics, generating ligand molecules that maintain realistic structures, high binding affinity, comparable drug-likeness and sythetic accessibility. The lightweight

Table 5: Summary of binding affinity and molecular properties of reference molecules and molecules generated by GeoAda and baselines. (↑) / (↓) denotes whether a larger / smaller number is preferred.

Methods	Vina Score (↓)		Vina Min (↓)		Vina Dock (↓)		High Affinity(↑)		QED(↑)		SA(↑)		Diversity(↑)	
	Avg.	Med.	Avg.	Med.	Avg.	Med.	Avg.	Med.	Avg.	Med.	Avg.	Med.	Avg.	Med.
liGAN [23]	-	-	-	-	-6.33	-6.20	21.1%	11.1%	0.39	0.39	0.59	0.57	0.66	0.67
GraphBP [17]	-	-	-	-	-4.80	-4.70	14.2%	6.7%	0.43	0.45	0.49	0.48	0.79	0.78
AR [19]	-5.75	-5.64	-6.18	-5.88	-6.75	-6.62	37.9%	31.0%	0.51	0.50	0.63	0.63	0.70	0.70
Pocket2Mol [22]	-5.14	-4.70	-6.42	-5.82	-7.15	-6.79	48.4%	51.0%	0.56	0.57	0.74	0.75	0.69	0.71
TargetDiff [8]	-5.47	-6.30	-6.64	-6.83	-7.80	-7.91	58.1%	59.1%	0.48	0.48	0.58	0.58	0.72	0.71
GeoAda (qm9)	-5.54	-6.31	-6.64	-6.46	-7.62	-7.64	57.4%	58.2%	0.49	0.51	0.58	0.58	0.74	0.75
GeoAda (Geom)	<u>-5.54</u>	-6.01	-6.68	-6.32	<u>-7.64</u>	<u>-7.71</u>	58.3%	59.3%	0.48	0.50	0.58	0.58	<u>0.76</u>	<u>0.75</u>
Reference	-6.36	-6.41	-6.71	-6.49	-7.45	-7.26	-	-	0.48	0.47	0.73	0.74	-	-

Table 6: Jensen-Shannon divergence of bond distance distributions between reference and generated molecules. (↓)

Bond	liGAN	AR	Pocket2Mol	TargetDiff	GeoAda (qm9)	GeoAda (Geom)
C-C	0.601	0.609	0.496	0.369	0.243	0.269
C=C	0.665	0.620	0.561	0.505	0.377	0.393
C-N	0.634	0.474	0.416	<u>0.363</u>	0.363	0.396
C=N	0.749	0.635	0.629	0.550	0.300	0.299
C-O	0.656	0.492	0.454	<u>0.421</u>	0.418	0.428
C=O	0.661	0.558	0.516	0.461	0.272	0.257
C-C	0.497	0.451	0.416	0.263	<u>0.305</u>	0.335
C=N	0.638	0.552	0.487	0.235	<u>0.297</u>	0.330

Table 7: Percentage of different ring sizes for reference and model generated molecules.

Ring Size	Ref.	liGAN	AR	Pocket2Mol	TargetDiff	GeoAda (qm9)	GeoAda (geom)
3	1.7%	28.1%	29.9%	0.1%	0.0%	0.0%	0.0%
4	0.0%	15.7%	0.0%	0.0%	2.8%	6.7%	5.8%
5	30.2%	29.8%	16.0%	16.4%	30.8%	47.2%	45.8%
6	67.4%	22.7%	51.2%	80.4%	50.7%	69.1%	78.2%
7	0.7%	2.6%	1.7%	2.6%	12.1%	23.5%	21.3%
8	0.0%	0.8%	0.7%	0.3%	5.3%	2.7%	4.7%
9	0.0%	0.3%	0.5%	0.1%	0.9%	3.8%	1.6%

adapter can inject subgraph (pocket) control into a broadly pretrained geometric diffusion model, achieving or surpassing task-specific baselines that rely on end-to-end training with protein context.

5.4 Ablations and Observations

Observation of the sudden convergence phenomenon Similar to the phenomenon observed in ControlNet [42], we also observe a *sudden convergence phenomenon* in our training process. As shown in Figure 5, between step 4500 and 4700, both training loss and validation MSE drop abruptly rather than gradually. To investigate this behavior, we conducted inference using the saved checkpoints from steps 3600 and 5600, and observed a notable performance jump between steps 4400 and 4800, which corresponds to significant reductions in ADE and FDE by 68.3% and 73.4%.

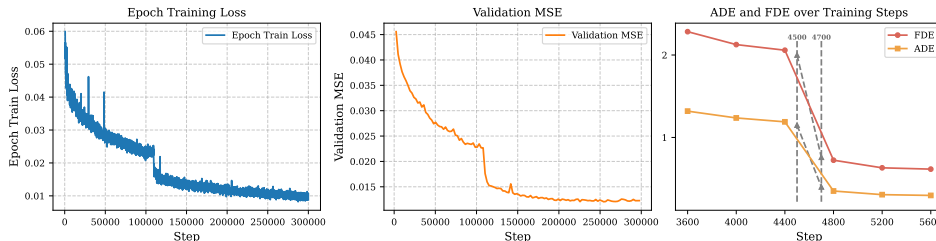


Figure 5: The sudden convergence phenomenon

Parameter efficiency analysis As shown in Appendix 9.3.1, we explore the impact of varying the number of equivariant zero layers. Increasing the number of trainable copy layers generally improves performance, but introduces more parameters and computational cost, revealing a trade-off between performance and efficiency. We also reported the number of tunable parameters for different tuning strategies in Table 21. Except for full fine-tuning, which is substantially larger, all other methods, including GeoAda, use comparable parameter sizes.

Ablation on Equivariant Zero Convolutions We evaluate two variants to assess the role of equivariant zero convolution: (1) replacing it with Gaussian-initialized standard convolutions, and (2) replacing each trainable copy with a single convolution layer (see App. 9.3.2). Both modifications result in notable performance drops, underscoring the importance of zero initialization and structural design for stable and effective fine-tuning.

6 Conclusion

We present GeoAda, a parameter-efficient and SE(3)-equivariant adapter framework for geometric diffusion models. It enables effective adaptation to diverse geometric control tasks without modifying the pretrained backbone, preserving both performance and geometric consistency.

References

- [1] Simon Axelrod and Rafael Gomez-Bombarelli. Geom, energy-annotated molecular conformations for property prediction and molecular generation. *Scientific Data*, 9(1):185, 2022. 8
- [2] Yen-Chi Cheng, Hsin-Ying Lee, Sergey Tulyakov, Alexander Schwing, and Liangyan Gui. Sdfusion: Multimodal 3d shape completion, reconstruction, and generation, 2023. 2
- [3] Stefan Chmiela, Alexandre Tkatchenko, Huziel E Sauceda, Igor Poltavsky, Kristof T Schütt, and Klaus-Robert Müller. Machine learning of accurate energy-conserving molecular force fields. *Science advances*, 3(5):e1603015, 2017. 1, 7
- [4] Allan dos Santos Costa, Ilan Mitnikov, Franco Pellegrini, Ameya Daigavane, Mario Geiger, Zhonglin Cao, Karsten Kreis, Tess Smidt, Emine Kucukbenli, and Joseph Jacobson. Equijump: Protein dynamics simulation via so(3)-equivariant stochastic interpolants, 2024. 3
- [5] Taoran Fang, Yunchao Zhang, Yang Yang, Chunping Wang, and Lei Chen. Universal prompt tuning for graph neural networks. *Advances in Neural Information Processing Systems*, 36:52464–52489, 2023. 3, 6, 7, 8, 16, 17, 18
- [6] Paul G Francoeur, Tomohide Masuda, Jocelyn Sunseri, Andrew Jia, Richard B Iovanisci, Ian Snyder, and David R Koes. Three-dimensional convolutional neural networks and a cross-docked data set for structure-based drug design. *Journal of chemical information and modeling*, 60(9):4200–4215, 2020. 8
- [7] Jiaqi Guan, Wesley Wei Qian, Xingang Peng, Yufeng Su, Jian Peng, and Jianzhu Ma. 3d equivariant diffusion for target-aware molecule generation and affinity prediction. In *The Eleventh International Conference on Learning Representations*, 2023. 1, 4
- [8] Jiaqi Guan, Wesley Wei Qian, Xingang Peng, Yufeng Su, Jian Peng, and Jianzhu Ma. 3d equivariant diffusion for target-aware molecule generation and affinity prediction. *arXiv preprint arXiv:2303.03543*, 2023. 8, 9
- [9] Jiaqi Han, Minkai Xu, Aaron Lou, Haotian Ye, and Stefano Ermon. Geometric trajectory diffusion models. *arXiv preprint arXiv:2410.13027*, 2024. 1, 3
- [10] Kaiming He, Xinlei Chen, Saining Xie, Yanghao Li, Piotr Dollár, and Ross Girshick. Masked autoencoders are scalable vision learners. In *Proceedings of the IEEE/CVF conference on computer vision and pattern recognition*, pages 16000–16009, 2022. 6, 7, 8, 16, 17, 18
- [11] Jonathan Ho, Ajay Jain, and Pieter Abbeel. Denoising diffusion probabilistic models. *Advances in neural information processing systems*, 33:6840–6851, 2020. 3, 6, 13
- [12] Emiel Hoogeboom, Victor Garcia Satorras, Clément Vignac, and Max Welling. Equivariant diffusion for molecule generation in 3d. In *International conference on machine learning*, pages 8867–8887. PMLR, 2022. 1, 3, 4
- [13] Zijie Huang, Wanjia Zhao, Jingdong Gao, Ziniu Hu, Xiao Luo, Yadi Cao, Yuanzhou Chen, Yizhou Sun, and Wei Wang. Physics-informed regularization for domain-agnostic dynamical system modeling. *arXiv preprint arXiv:2410.06366*, 2024. 1
- [14] Menglin Jia, Luming Tang, Bor-Chun Chen, Claire Cardie, Serge Belongie, Bharath Hariharan, and Ser-Nam Lim. Visual prompt tuning. In *European conference on computer vision*, pages 709–727. Springer, 2022. 6
- [15] Thomas Kipf, Ethan Fetaya, Kuan-Chieh Wang, Max Welling, and Richard Zemel. Neural relational inference for interacting systems. *arXiv preprint arXiv:1802.04687*, 2018. 1, 6
- [16] Shengrui Li, Xueting Han, and Jing Bai. Adapterggnn: Parameter-efficient fine-tuning improves generalization in gnns, 2023. 3
- [17] Meng Liu, Youzhi Luo, Kanji Uchino, Koji Maruhashi, and Shuiwang Ji. Generating 3d molecules for target protein binding. In *International Conference on Machine Learning*, 2022. 9

- [18] Zemin Liu, Xingtong Yu, Yuan Fang, and Xinming Zhang. Graphprompt: Unifying pre-training and downstream tasks for graph neural networks, 2023. 3
- [19] Shitong Luo, Jiaqi Guan, Jianzhu Ma, and Jian Peng. A 3d generative model for structure-based drug design. *Advances in Neural Information Processing Systems*, 34, 2021. 9
- [20] Yanchen Luo, Junfeng Fang, Sihang Li, Zhiyuan Liu, Jiancan Wu, An Zhang, Wenjie Du, and Xiang Wang. Text-guided diffusion model for 3d molecule generation. *arXiv preprint arXiv:2410.03803*, 2024. 4
- [21] Alex Morehead and Jianlin Cheng. Geometry-complete diffusion for 3d molecule generation and optimization, 2024. 1, 2
- [22] Xingang Peng, Shitong Luo, Jiaqi Guan, Qi Xie, Jian Peng, and Jianzhu Ma. Pocket2mol: Efficient molecular sampling based on 3d protein pockets. *arXiv preprint arXiv:2205.07249*, 2022. 9
- [23] Matthew Ragoza, Tomohide Masuda, and David Ryan Koes. Generating 3D molecules conditional on receptor binding sites with deep generative models. *Chem Sci*, 13:2701–2713, Feb 2022. 9
- [24] Raghunathan Ramakrishnan, Pavlo O Dral, Matthias Rupp, and O Anatole Von Lilienfeld. Quantum chemistry structures and properties of 134 kilo molecules. *Scientific data*, 1(1):1–7, 2014. 8
- [25] Hyunwoo Ryu, Jiwoo Kim, Hyunseok An, Junwoo Chang, Joohwan Seo, Taehan Kim, Yubin Kim, Chaewon Hwang, Jongeun Choi, and Roberto Horowitz. Diffusion-edfs: Bi-equivariant denoising generative modeling on se(3) for visual robotic manipulation, 2023. 1, 2
- [26] Victor Garcia Satorras, Emiel Hooeboom, and Max Welling. E(n) equivariant graph neural networks. *arXiv preprint arXiv:2102.09844*, 2021. 1, 6
- [27] Kristof Schütt, Oliver Unke, and Michael Gastegger. Equivariant message passing for the prediction of tensorial properties and molecular spectra. In *International Conference on Machine Learning*, pages 9377–9388. PMLR, 2021. 7
- [28] Chence Shi, Shitong Luo, Minkai Xu, and Jian Tang. Learning gradient fields for molecular conformation generation. In *International conference on machine learning*, pages 9558–9568. PMLR, 2021. 7
- [29] Yang Song and Stefano Ermon. Generative modeling by estimating gradients of the data distribution. *Advances in neural information processing systems*, 32, 2019. 3
- [30] Yang Song, Jascha Sohl-Dickstein, Diederik P Kingma, Abhishek Kumar, Stefano Ermon, and Ben Poole. Score-based generative modeling through stochastic differential equations. In *International Conference on Learning Representations*, 2021. 3
- [31] Charles Stein. A bound for the error in the normal approximation to the distribution of a sum of dependent random variables. In *Proceedings of the sixth Berkeley symposium on mathematical statistics and probability, volume 2: Probability theory*, volume 6, pages 583–603. University of California Press, 1972. 3
- [32] Mingchen Sun, Kaixiong Zhou, Xin He, Ying Wang, and Xin Wang. Gppt: Graph pre-training and prompt tuning to generalize graph neural networks. In *Proceedings of the 28th ACM SIGKDD Conference on Knowledge Discovery and Data Mining*, KDD ’22, page 1717–1727, New York, NY, USA, 2022. Association for Computing Machinery. 3
- [33] Masatoshi Uehara, Yulai Zhao, Kevin Black, Ehsan Hajiramezanali, Gabriele Scalia, Nathaniel Lee Diamant, Alex M Tseng, Tommaso Biancalani, and Sergey Levine. Fine-tuning of continuous-time diffusion models as entropy-regularized control, 2024. 3
- [34] Julen Urain, Niklas Funk, Jan Peters, and Georgia Chalvatzaki. Se(3)-diffusionfields: Learning smooth cost functions for joint grasp and motion optimization through diffusion, 2023. 1, 2

- [35] Bram Wallace, Meihua Dang, Rafael Rafailov, Linqi Zhou, Aaron Lou, Senthil Purushwalkam, Stefano Ermon, Caiming Xiong, Shafiq Joty, and Nikhil Naik. Diffusion model alignment using direct preference optimization, 2023. 3
- [36] Zhendong Wang, Yifan Jiang, Yadong Lu, yelong shen, Pengcheng He, Weizhu Chen, Zhangyang Wang, and Mingyuan Zhou. In-context learning unlocked for diffusion models. In *Thirty-seventh Conference on Neural Information Processing Systems*, 2023. 1, 3
- [37] Can Xu, Haosen Wang, Weigang Wang, Pengfei Zheng, and Hongyang Chen. Geometric-facilitated denoising diffusion model for 3d molecule generation. In *Proceedings of the AAAI Conference on Artificial Intelligence*, 2024. 1, 2
- [38] Chenxin Xu, Robby T Tan, Yuhong Tan, Siheng Chen, Yu Guang Wang, Xinchao Wang, and Yanfeng Wang. Eqmotion: Equivariant multi-agent motion prediction with invariant interaction reasoning. In *Proceedings of the IEEE/CVF Conference on Computer Vision and Pattern Recognition*, pages 1410–1420, 2023. 6, 7
- [39] Minkai Xu, Alexander Powers, Ron Dror, Stefano Ermon, and Jure Leskovec. Geometric latent diffusion models for 3d molecule generation. In *International Conference on Machine Learning*. PMLR, 2023. 1, 2
- [40] Minkai Xu, Lantao Yu, Yang Song, Chence Shi, Stefano Ermon, and Jian Tang. Geodiff: A geometric diffusion model for molecular conformation generation. In *International Conference on Learning Representations*, 2022. 1, 2, 3
- [41] Pei Xu, Jean-Bernard Hayet, and Ioannis Karamouzas. Socialvae: Human trajectory prediction using timewise latents. In *European Conference on Computer Vision*, pages 511–528. Springer, 2022. 6
- [42] Lvmin Zhang, Anyi Rao, and Maneesh Agrawala. Adding conditional control to text-to-image diffusion models. In *Proceedings of the IEEE/CVF international conference on computer vision*, pages 3836–3847, 2023. 1, 2, 3, 5, 9
- [43] Richard Zhang, Phillip Isola, and Alexei A Efros. Colorful image colorization. In *Computer Vision—ECCV 2016: 14th European Conference, Amsterdam, The Netherlands, October 11–14, 2016, Proceedings, Part III 14*, pages 649–666. Springer, 2016. 5, 6

Appendix

7 Proof

Below is the explanation and proof of Proposition 4.1:

Proof. Since ϵ_θ is SE(3)-equivariant by assumption, we have for any $h \in \text{SE}(3)$,

$$\epsilon_\theta(h \cdot \mathcal{G}') = h \cdot \epsilon_\theta(\mathcal{G}'), \quad \text{where } \mathcal{G}' = \mathbf{f}(\mathcal{G}_\tau, \mathcal{C}).$$

We consider each component:

- The coupling operator \mathbf{f} augments \mathcal{G}_τ with control \mathcal{C} in a way that respects the SE(3) structure: global controls modify features invariantly; subgraph controls are merged geometrically; frame controls concatenate along the temporal axis. Thus, \mathbf{f} is SE(3)-equivariant.
- The decoupling operator \mathbf{g} selects a subset of nodes or frames without altering their coordinates. Therefore, it commutes with SE(3) action: $\mathbf{g}(h \cdot \mathcal{G}'') = h \cdot \mathbf{g}(\mathcal{G}'')$.

Combining the above, we explicitly see that for any $h \in \text{SE}(3)$ defined as $h(\mathbf{x}) = R\mathbf{x} + \mathbf{d}$, we have:

$$\begin{aligned} & \mathbf{g} \circ \epsilon_\theta \circ \mathbf{f}(h \cdot (\mathcal{G}_\tau, \mathcal{C})) \\ &= \mathbf{g}(\epsilon_\theta(h \cdot \mathbf{f}(\mathcal{G}_\tau, \mathcal{C}))) \\ &= \mathbf{g}(h \cdot \epsilon_\theta(\mathbf{f}(\mathcal{G}_\tau, \mathcal{C}))) \\ &= h \cdot \mathbf{g}(\epsilon_\theta(\mathbf{f}(\mathcal{G}_\tau, \mathcal{C}))) \\ &= R \cdot (\mathbf{g} \circ \epsilon_\theta \circ \mathbf{f}(\mathcal{G}_\tau, \mathcal{C})) + \mathbf{d} \\ &= h \cdot (\mathbf{g} \circ \epsilon_\theta \circ \mathbf{f}(\mathcal{G}_\tau, \mathcal{C})) \end{aligned}$$

Therefore, the composed function $\mathbf{g} \circ \epsilon_\theta \circ \mathbf{f}$ is SE(3)-equivariant. □

8 More Details on Experiments

8.1 Hyper-parameters

We provide the detailed hyper-parameters of GeoAda in Table 8. We adopt Adam optimizer with betas (0.9, 0.999) and $\epsilon = 10^{-8}$. For all experiments, we use the linear noise schedule per [11] with $\beta_{\text{start}} = 0.02$ and $\beta_{\text{end}} = 0.0001$.

Table 8: Hyper-parameters of GeoAda in the experiments.

	n_layer	hidden	time_emb_dim	\mathcal{T}	batch_size	learning_rate
N-body	6	128	32	1000	128	0.0001
MD	6	128	32	1000	128	0.0001
CMU Mocap	6	64	32	100	128	0.0001

8.2 Baselines

Full FT.

Full FT fully fine-tunes the pre-trained model f during downstream training. The entire model is updated to fit the target task.

PARTIAL- k .

PARTIAL- k fine-tunes only the last k layers of the model f , while freezing the remaining layers. This method balances adaptability with parameter efficiency by limiting the number of updated layers.

Graph Prompt Feature (GPF).

In **GPF**, the pre-trained encoder f is kept frozen, and a learnable prompt vector p is injected into the input feature space. During training, only the prompt vector p and the prediction head θ are optimized. This method enables task adaptation through a lightweight, task-specific prompt without modifying the backbone model. In our implementation, we replace the original MLP head with a three-layer Equivariant Geometric Trajectory Network (EGTN), which ensures the projection head maintains geometric consistency with the model.

Graph Prompt Feature-Plus (GPF-plus).

Extending GPF, this variant constructs node-wise prompt vectors using k learnable basis vectors p_1^b, \dots, p_k^b and a set of learnable linear weights a_1, \dots, a_k . These components are used to compute node-specific prompts p_i via a compositional mechanism. The model f remains frozen, while prediction head θ , learnable basis vectors p_i^b , and learnable linear weights a_i are optimized.

Prompt-Template

We prepend a learnable prompt layer(Equivariant Geometric Trajectory Network) to adapt new inputs to the distribution seen during pretraining, following with prediction head θ .

MLP- k (EGTN- k).

This baseline freezes the entire pre-trained model f and replaces the prediction head with a k -layer multilayer perceptron (MLP). To preserve equivariance in our setting, we replace the MLP with an Equivariant Geometric Trajectory Network (EGTN) block. Only the EGTN-based head is trained during the downstream task.

8.3 Details of the datasets

8.3.1 Global Type Control

Pretrain Dataset The statistics of the pretrained datasets on Global Type Control are presented in Table. 9.

Table 9: Pretrain Dataset statistics by Global Type.

Type	Washwindow	Directing Traffic	Basketball Signal	Pretrain
train	12126	9557	7776	29459
val	1342	2346	1920	5588
test	1342	2346	1920	5588

Downstream datasets The statistics of the downstream datasets utilized for the models pretrained on Global Type Control are presented in Table. 10.

Table 10: Downstream Dataset statistics by Global Type.

Type	Running	Walking	Jumping	Basketball	Soccer
train	245	869	1345	1044	1210
val	47	145	1008	254	264
test	47	145	1008	254	264

8.4 Model

8.4.1 Geometric Trajectory Diffusion Models

Unconditional Generation For unconditional generation, we model the trajectory distribution subject to SE(3)-invariance. The following theorem provides constraints for the prior and transition kernel.

Theorem 8.1. *If the prior $p_{\mathcal{T}}(\mathbf{x}_{\mathcal{T}}^{[T]})$ is $SE(3)$ -invariant, and the transition kernels $p_{\tau-1}(\mathbf{x}_{\tau-1}^{[T]} | \mathbf{x}_{\tau}^{[T]})$, $\forall \tau \in \{1, \dots, \mathcal{T}\}$ are $SE(3)$ -equivariant, then the marginal $p_{\tau}(\mathbf{x}_{\tau}^{[T]})$ at any step $\tau \in \{0, \dots, \mathcal{T}\}$ is also $SE(3)$ -invariant.*

Prior in the translation-invariant subspace. The prior is built on a translation-invariant subspace $\mathcal{X}_{\mathbf{P}} \subset \mathcal{X}$, induced by a linear transformation \mathbf{P} :

$$\mathbf{P} = \mathbf{I}_D \otimes \left(\mathbf{I}_{TN} - \frac{1}{TN} \mathbf{1}_{TN} \mathbf{1}_{TN}^{\top} \right)$$

which results in a restricted Gaussian distribution supported only on the subspace, denoted $\tilde{\mathcal{N}}(\mathbf{0}, \mathbf{I})$, and is isotropic and $SO(3)$ -invariant. To sample, one samples from $\mathcal{N}(\mathbf{0}, \mathbf{I})$ and projects it onto the subspace.

Transition kernel. The transition kernel is parameterized in the subspace $\mathcal{X}_{\mathbf{P}}$, given by:

$$p_{\theta}(\tilde{\mathbf{x}}_{\tau-1}^{[T]} | \tilde{\mathbf{x}}_{\tau}^{[T]}) = \tilde{\mathcal{N}}(\tilde{\boldsymbol{\mu}}_{\theta}(\tilde{\mathbf{x}}_{\tau}^{[T]}, \tau), \sigma_{\tau}^2 \mathbf{I})$$

where the mean function $\tilde{\boldsymbol{\mu}}_{\theta}$ is $SO(3)$ -equivariant. The function is re-parameterized as:

$$\tilde{\boldsymbol{\mu}}_{\theta}(\tilde{\mathbf{x}}_{\tau}^{[T]}, \tau) = \frac{1}{\sqrt{\alpha_{\tau}}} \left(\tilde{\mathbf{x}}_{\tau}^{[T]} - \frac{\beta_{\tau}}{\sqrt{1 - \alpha_{\tau}}} \tilde{\boldsymbol{\epsilon}}_{\theta}(\mathbf{x}_{\tau}^{[T]}, \tau) \right)$$

where $\tilde{\boldsymbol{\epsilon}}_{\theta} = P \circ \mathbf{f}_{\theta}$ is an $SO(3)$ -equivariant adaptation of the proposed EGTN.

Training and inference. The VLB is optimized for training, with the objective:

$$\mathcal{L}_{\text{uncond}} := \mathbb{E}_{\mathbf{x}_0^{[T]}, \tilde{\boldsymbol{\epsilon}} \sim \tilde{\mathcal{N}}(\mathbf{0}, \mathbf{I}), \tau \sim \text{Unif}(1, \mathcal{T})} \left[\|\tilde{\boldsymbol{\epsilon}} - \tilde{\boldsymbol{\epsilon}}_{\theta}(\tilde{\mathbf{x}}_{\tau}^{[T]}, \tau)\|^2 \right]$$

The inference process involves projecting intermediate samples onto the subspace $\mathcal{X}_{\mathbf{P}}$.

Conditional Generation In conditional generation, the target distribution is $SE(3)$ -equivariant with respect to the given frames. The following theorem provides constraints for the prior and transition kernel.

Theorem 8.2. *If the prior $p_{\mathcal{T}}(\mathbf{x}_{\mathcal{T}}^{[T]} | \mathbf{x}_c^{[T_c]})$ is $SE(3)$ -equivariant, and the transition kernels $p_{\tau-1}(\mathbf{x}_{\tau-1}^{[T]} | \mathbf{x}_{\tau}^{[T]}, \mathbf{x}_c^{[T_c]})$, $\forall \tau \in \{1, \dots, \mathcal{T}\}$ are $SE(3)$ -equivariant, the marginal $p_{\tau}(\mathbf{x}_{\tau}^{[T]} | \mathbf{x}_c^{[T_c]})$, $\forall \tau \in \{0, \dots, \mathcal{T}\}$ is $SE(3)$ -equivariant.*

Flexible equivariant prior. We provide a guideline for distinguishing feasible prior designs. The prior $\mathcal{N}(\boldsymbol{\mu}(\mathbf{x}_c^{[T_c]}), \mathbf{I})$ is $SE(3)$ -equivariant if $\boldsymbol{\mu}(\mathbf{x}_c^{[T_c]})$ is $SE(3)$ -equivariant. The mean function $\boldsymbol{\mu}(\mathbf{x}_c^{[T_c]})$ serves as an anchor to transition geometric information from the given frames to the target distribution. For instance, the anchor can be defined as:

$$\mathbf{x}_r^{[T]} = \mathbf{1}_{T \times N} \otimes \sum_{s \in [T_c]} w^{(s)} \bar{\mathbf{x}}_c^{(s)}$$

where the weights satisfy $\sum_{s \in [T_c]} w^{(s)} = 1$.

The weights $\mathbf{w}^{(t,s)}$ are derived as:

$$\mathbf{W}_{t,s} = [\boldsymbol{\gamma} \otimes \hat{\mathbf{h}}_c^{[T_c]}]_{t,s} \in \mathbb{R}^N, \quad \mathbf{w}^{(t,s)} = \begin{cases} \mathbf{W}_{t,s} & \text{if } s < T_c - 1, \\ \mathbf{1}_N - \sum_{s=0}^{T_c-2} \mathbf{W}_{t,s} & \text{if } s = T_c - 1. \end{cases}$$

where $\boldsymbol{\gamma} \in \mathbb{R}^T$ are learnable parameters, ensuring the constraint for translation equivariance.

Transition kernel. To match the proposed prior, we modify both the forward and reverse processes. The forward process is defined as:

$$q(\mathbf{x}_{\tau}^{[T]} | \mathbf{x}_{\tau-1}^{[T]}, \mathbf{x}_c^{[T_c]}) := \mathcal{N}(\mathbf{x}_{\tau}^{[T]}; \mathbf{x}_r + \sqrt{1 - \beta_{\tau}}(\mathbf{x}_{\tau-1}^{[T]} - \mathbf{x}_r), \beta_{\tau} \mathbf{I}),$$

which ensures that $q(\mathbf{x}_{\tau}^{[T]} | \mathbf{x}_c^{[T_c]})$ matches the equivariant prior \mathbf{x}_r . The reverse transition kernel is:

$$p_{\tau-1}(\mathbf{x}_{\tau-1}^{[T]} | \mathbf{x}_{\tau}^{[T]}, \mathbf{x}_c^{[T_c]}) = \mathcal{N}(\boldsymbol{\mu}_{\theta}(\mathbf{x}_{\tau}^{[T]}, \tau, \mathbf{x}_c^{[T_c]}), \sigma_{\tau}^2 \mathbf{I}).$$

We adopt the noise prediction objective for the reverse process, rewriting μ_θ as:

$$\mu_\theta(\mathbf{x}_\tau^{[T]}, \mathbf{x}_c^{[T_c]}, \tau) = \mathbf{x}_\tau^{[T]} + \frac{1}{\sqrt{\alpha_\tau}} \left(\mathbf{x}_\tau^{[T]} - \mathbf{x}_\tau^{[T]} - \frac{\beta_\tau}{\sqrt{1-\alpha_\tau}} \epsilon_\theta(\mathbf{x}_\tau^{[T]}, \mathbf{x}_c^{[T_c]}, \tau) \right),$$

where the denoising network ϵ_θ is implemented as an EGTN with translation invariance, ensuring the translation equivariance of μ_θ .

Training and inference. Optimizing the VLB of our diffusion model leads to the following objective:

$$\mathcal{L}_{\text{cond}} := \mathbb{E}_{\mathbf{x}_0^{[T]}, \mathbf{x}_c^{[T_c]}, \epsilon \sim \mathcal{N}(\mathbf{0}, \mathbf{I}), \tau \sim \text{Unif}(1, T)} \left[\|\epsilon - \epsilon_\theta(\mathbf{x}_\tau^{[T]}, \mathbf{x}_c^{[T_c]}, \tau)\|^2 \right].$$

8.5 Evaluation Metrics in the Unconditional Case

All these metrics are evaluated on a set of model samples with the same size as the testing set.

Marginal score is computed as the absolute difference of two empirical probability density functions. Practically, we collect the x, y, z coordinates at each time step marginalized over all nodes in all systems in the predictions and the ground truth (testing set). Then we split the collection into 50 bins and compute the MAE in each bin, finally averaged across all time steps to obtain the score. Note that on MD17, instead of computing the pdf on coordinates, we compute the pdf on the length of the chemical bonds, which is a clearer signal that correlates to the validity of the generated MD trajectory, since during MD simulation the bond lengths are usually stable with very small vibrations. Marginal score gives a broad statistical measurement how each dimension of the generated samples align with the original data.

Classification score is computed as the cross-entropy loss of a sequence classification model that aims to distinguish whether the trajectory is generated by the model or from the testing set. To be specific, we construct a dataset mixed by the generated samples and the testing set, and randomly split it into 80% and 20% subsets for training and testing. Then the model is trained on the training set and the classification score is computed as the cross-entropy on the testing set. We use a 1-layer EqMotion with a classification head as the model. The classification score provided intuition on how difficult it is to distinguish the generated samples and the original data.

Prediction score is computed as the MSE loss of a train-on-synthetic-test-on-real sequence to sequence model. In detail, we train a 1-layer EqMotion on the sampled dataset with the task of predicting the second half of the trajectory given the first half. We then evaluate the model on the testing set and report the MSE as the prediction score. Prediction score provides intuition on the capability of the generative model on generating synthetic data that well aligns with the ground truth.

9 More Experiments and Discussions

9.1 Molecular

Additional experimental results on the Malonaldehyde and Naphthalene are shown below:

Table 11: Comparisons for Molecular Dynamics prediction on MD17 dataset (all results reported by $\times 10^{-1}$). The best results are highlighted in bold. Results averaged over 5 runs

Scenarios	Malonaldehyde				Naphthalene			
	FT		Pretrain		FT		Pretrain	
	ADE	FDE	ADE	FDE	ADE	FDE	ADE	FDE
Pretrain	3.235 \pm 0.012	5.189 \pm 0.023	0.962 \pm 0.007	1.584 \pm 0.021	1.416 \pm 0.003	2.268 \pm 0.005	0.714 \pm 0.002	0.972 \pm 0.006
FT	0.897 \pm 0.002	1.511 \pm 0.009	1.405 \pm 0.006	2.237 \pm 0.023	0.555 \pm 0.001	0.867 \pm 0.010	nan	nan
PARTIAL-k [10]	0.981 \pm 0.004	1.675 \pm 0.015	1.230 \pm 0.003	2.110 \pm 0.006	0.653 \pm 0.002	0.903 \pm 0.003	2.083 \pm 0.009	1.629 \pm 0.007
MLP-k	0.997 \pm 0.005	1.694 \pm 0.010	1.291 \pm 0.004	2.051 \pm 0.015	0.718 \pm 0.001	0.969 \pm 0.005	nan	nan
Prompt-Tem	1.092 \pm 0.019	2.003 \pm 0.056	2.323 \pm 0.024	3.351 \pm 0.081	0.972 \pm 0.006	1.593 \pm 0.021	nan	nan
GPF [5]	1.176 \pm 0.012	1.931 \pm 0.030	282.1 \pm 157.9/inf	24.97 \pm 24.43/inf	0.758 \pm 0.002	1.005 \pm 0.005	nan	nan
GPF-plus [5]	1.018 \pm 0.003	1.793 \pm 0.010	3.527 \pm 0.501	4.719 \pm 1.397	0.717 \pm 0.003	0.873 \pm 0.006	1.891 \pm 0.056	2.674 \pm 0.156
GeoAda	0.862 \pm 0.002	1.414 \pm 0.014	0.963 \pm 0.007	1.573 \pm 0.018	0.581 \pm 0.002	0.822 \pm 0.004	0.714 \pm 0.001	0.969 \pm 0.007

9.2 Human Motion

Additional experimental results on the *jumping* and *soccer* scenarios are presented below. We also report the standard deviations across all experiments.

Table 12: Short-term prediction on **running** from the CMU Mocap dataset.

scenarios	running				pretrain			
	80	160	320	400	80	160	320	400
Pretrain	28.74 \pm 0.34	57.99 \pm 0.33	126.20 \pm 0.93	159.37 \pm 1.15	7.941 \pm 0.02	16.84 \pm 0.04	39.91 \pm 0.43	52.45 \pm 0.07
Full FT	20.34 \pm 0.32	35.26 \pm 0.19	60.58 \pm 1.14	70.20 \pm 1.36	nan	nan	nan	nan
PARTIAL- <i>k</i>	20.47 \pm 0.32	36.04 \pm 0.40	68.15 \pm 0.70	82.59 \pm 0.86	nan	nan	nan	nan
MLP- <i>k</i>	23.35 \pm 0.39	44.44 \pm 0.71	84.27 \pm 1.58	101.42 \pm 2.11	nan	nan	nan	nan
GPF	19.17 \pm 0.28	32.85 \pm 0.66	52.83 \pm 1.03	60.90 \pm 1.54	21.38 \pm 0.97	35.44 \pm 1.05	65.23 \pm 1.76	79.55 \pm 1.11
GPF-plus	19.11 \pm 0.54	31.93 \pm 0.81	49.85 \pm 1.21	56.67 \pm 1.39	nan	nan	nan	nan
GeoAda	18.70 \pm 0.37	33.56 \pm 0.25	<u>50.26</u> \pm 0.42	55.54 \pm 0.36	<u>7.972</u> \pm 0.02	<u>16.91</u> \pm 0.05	<u>40.06</u> \pm 0.42	<u>52.61</u> \pm 0.07

Table 13: Short-term prediction on **walking** from the CMU Mocap dataset.

scenarios	walking				pretrain			
	80	160	320	400	80	160	320	400
Pretrain	15.49 \pm 0.07	30.66 \pm 0.16	68.71 \pm 0.33	89.23 \pm 0.43	<u>7.941</u> \pm 0.02	16.84 \pm 0.04	39.91 \pm 0.43	52.45 \pm 0.07
Full FT	<u>10.01</u> \pm 0.17	<u>15.12</u> \pm 0.14	<u>23.98</u> \pm 0.13	<u>28.49</u> \pm 0.19	nan	nan	nan	nan
PARTIAL- <i>k</i>	10.47 \pm 0.81	16.97 \pm 0.43	30.97 \pm 0.60	37.69 \pm 0.60	17.26 \pm 0.23	31.75 \pm 0.36	66.29 \pm 0.44	84.27 \pm 0.79
MLP- <i>k</i>	10.86 \pm 1.07	18.74 \pm 1.37	35.78 \pm 1.92	44.86 \pm 1.35	nan	nan	nan	nan
GPF	10.79 \pm 0.14	16.79 \pm 0.16	28.32 \pm 0.21	33.48 \pm 0.22	22.04 \pm 0.38	37.10 \pm 0.40	71.24 \pm 0.39	88.23 \pm 0.97
GPF-plus	10.17 \pm 0.16	16.23 \pm 0.12	26.29 \pm 0.22	31.54 \pm 0.19	nan	nan	nan	nan
GeoAda	8.92 \pm 1.02	13.82 \pm 1.26	22.99 \pm 1.30	26.68 \pm 1.31	7.932 \pm 0.03	<u>16.90</u> \pm 0.04	38.96 \pm 0.47	<u>52.54</u> \pm 0.10

Table 14: Short-term prediction comparison on the **basketball** action from the CMU Mocap dataset.

scenarios	basketball				pretrain			
	80	160	320	400	80	160	320	400
Pretrain	17.92 \pm 0.06	35.89 \pm 0.12	78.48 \pm 0.47	101.12 \pm 0.69	<u>7.941</u> \pm 0.02	<u>16.84</u> \pm 0.04	<u>39.91</u> \pm 0.43	52.45 \pm 0.07
FT	16.95 \pm 0.11	30.33 \pm 0.17	58.28 \pm 0.41	71.93 \pm 0.54	-	-	-	-
PARTIAL- <i>k</i>	17.54 \pm 0.12	32.03 \pm 0.43	62.96 \pm 0.86	78.95 \pm 0.98	-	-	-	-
MLP- <i>k</i>	17.60 \pm 0.50	34.76 \pm 1.26	72.90 \pm 2.36	86.34 \pm 1.53	-	-	-	-
GPF	18.48 \pm 0.09	31.94 \pm 0.14	58.80 \pm 0.28	73.56 \pm 0.29	21.38 \pm 0.11	35.44 \pm 0.27	65.23 \pm 0.30	79.55 \pm 0.51
GPF-plus	17.17 \pm 0.07	31.86 \pm 0.15	58.48 \pm 0.32	72.71 \pm 0.24	-	-	-	-
GeoAda	16.85 \pm 0.24	29.71 \pm 0.41	57.59 \pm 0.39	71.19 \pm 0.48	7.898 \pm 0.05	16.79 \pm 0.05	39.70 \pm 0.04	52.50 \pm 0.07

Table 15: Short-term prediction comparison on the **jumping** action from the CMU Mocap dataset.

scenarios	jumping				pretrain			
	80	160	320	400	80	160	320	400
Pretrain	-	-	-	-	7.941 \pm 0.02	<u>16.84</u> \pm 0.04	<u>39.91</u> \pm 0.43	52.45 \pm 0.07
FT	-	-	-	-	26.67 \pm 0.10	50.83 \pm 0.29	94.13 \pm 0.58	112.66 \pm 0.71
PARTIAL- <i>k</i>	26.01 \pm 0.08	49.19 \pm 0.09	95.84 \pm 0.13	116.24 \pm 0.23	19.08 \pm 0.17	38.53 \pm 0.34	79.77 \pm 0.52	99.85 \pm 1.07
MLP- <i>k</i>	22.63/nan	44.68/nan	88.93/nan	108.43/nan	15.32 \pm 0.30	31.92 \pm 0.26	66.50 \pm 0.42	82.55 \pm 0.93
GPF	28.74 \pm 0.19	51.97 \pm 0.19	97.80 \pm 0.34	117.94 \pm 0.37	\pm 0.08 -	-	-	-
GPF-plus	-	-	-	-	-	-	-	-
GeoAda	25.91 \pm 0.09	48.83 \pm 0.83	91.51 \pm 0.07	109.24 \pm 0.60	<u>7.956</u> \pm 0.03	16.82 \pm 0.04	39.55 \pm 0.47	<u>52.57</u> \pm 0.09

Table 16: Short-term prediction comparison on the **soccer** action from the CMU Mocap dataset.

scenarios	soccer				pretrain			
	80	160	320	400	80	160	320	400
Pretrain	-	-	-	-	7.941 \pm 0.02	16.84 \pm 0.04	<u>39.91</u> \pm 0.43	<u>52.45</u> \pm 0.07
FT	17.65 \pm 0.17	31.43 \pm 0.35	59.76 \pm 0.44	74.30 \pm 0.54	-	-	-	-
PARTIAL- <i>k</i>	18.83 \pm 0.10	32.86 \pm 0.07	64.58 \pm 0.37	81.53 \pm 0.50	14.14 \pm 0.41	24.95 \pm 0.38	50.89 \pm 0.40	64.24 \pm 0.51
MLP- <i>k</i>	-	-	-	-	-	-	-	-
GPF	19.28 \pm 0.10	32.18 \pm 0.14	69.58 \pm 0.42	73.63 \pm 0.63	15.70 \pm 0.30	28.31 \pm 0.28	58.57 \pm 0.42	74.28 \pm 0.61
GPF-plus	19.11 \pm 0.18	32.03 \pm 0.31	59.67 \pm 0.46	74.25 \pm 0.65	15.22 \pm 0.23	26.22 \pm 0.29	52.02 \pm 0.47	65.17 \pm 0.53
GeoAda	17.04 \pm 0.14	30.03 \pm 0.12	53.51 \pm 0.25	64.78 \pm 0.42	<u>7.961</u> \pm 0.02	<u>16.90</u> \pm 0.03	39.46 \pm 0.41	52.43 \pm 0.09

Table 17: Long-term prediction on CMU Mocap: **Running** and **Walking**.

scenarios	running		pretrain		walking		pretrain	
	560	1000	560	1000	560	1000	560	1000
Pretrain	219.16 \pm 2.18	314.85 \pm 3.03	77.06 \pm 0.47	<u>130.51</u> \pm 0.27	129.43 \pm 0.77	212.94 \pm 1.90	77.06 \pm 0.47	<u>130.51</u> \pm 0.27
Full FT	85.14 \pm 2.36	97.02 \pm 1.45	nan	nan	36.92 \pm 1.37	52.58 \pm 0.62	nan	nan
PARTIAL- <i>k</i> [10]	102.85 \pm 1.68	108.47 \pm 2.03	nan	nan	51.36 \pm 1.93	84.72 \pm 0.67	118.82 \pm 0.58	182.88 \pm 0.79
MLP- <i>k</i>	127.67 \pm 2.46	131.59 \pm 2.90	nan	nan	62.97 \pm 1.45	102.34 \pm 0.86	nan	nan
GPF [5]	61.92 \pm 1.02	71.42 \pm 1.27	nan	nan	42.37 \pm 0.31	52.24 \pm 0.38	119.43 \pm 0.60	171.74 \pm 0.55
GPF-plus [5]	63.56 \pm 1.54	71.60 \pm 0.95	nan	nan	41.31 \pm 0.35	56.47 \pm 0.4	nan	nan
GeoAda	60.88 \pm 0.82	70.22 \pm 0.20	<u>77.22</u> \pm 0.45	130.17 \pm 0.26	34.52 \pm 2.26	50.49 \pm 0.33	<u>78.12</u> \pm 0.49	129.97 \pm 0.30

Table 18: Long-term prediction on CMU Mocap: **Jumping and Soccer.**

scenarios	jumping		pretrain		soccer		pretrain	
	560	1000	560	1000	560	1000	560	1000
Pretrain	—	—	77.06 ± 0.47	130.51 ± 0.27	—	—	77.06 ± 0.47	130.51 ± 0.27
Full FT	—	—	145.76 ± 1.23	199.34 ± 2.01	101.44 ± 0.51	157.11 ± 0.96	—	—
PARTIAL- k [10]	149.06 ± 0.37	181.52 ± 0.81	135.25 ± 0.92	186.16 ± 1.58	113.88 ± 0.75	170.50 ± 1.98	89.63 ± 1.62	142.41 ± 1.84
MLP- k	$140.11/\text{nan}$	$184.77/\text{nan}$	111.71 ± 0.74	158.55 ± 1.37	—	—	—	—
GPF [5]	151.50 ± 0.65	194.94 ± 0.34	—	—	100.23 ± 0.88	151.84 ± 1.23	104.03 ± 0.81	161.56 ± 1.31
GPF-plus [5]	—	—	—	—	101.15 ± 0.86	153.43 ± 0.79	90.12 ± 1.10	142.30 ± 1.12
GeoAda	139.46 ± 0.29	184.01 ± 0.60	76.98 ± 0.51	130.72 ± 0.26	84.91 ± 0.46	125.91 ± 0.75	77.19 ± 0.48	130.06 ± 0.31

Table 19: Long-term prediction on CMU Mocap: **Basketball.**

scenarios	basketball		pretrain	
	560	1000	560	1000
Pretrain	143.49 ± 1.19	223.99 ± 2.23	77.06 ± 0.47	130.51 ± 0.27
Full FT	94.59 ± 0.58	132.34 ± 1.30	nan	nan
PARTIAL- k [10]	106.84 ± 1.00	146.27 ± 1.24	nan	nan
MLP- k	107.30 ± 2.76	149.58 ± 2.24	nan	nan
GPF [5]	97.16 ± 0.35	128.29 ± 0.43	nan	nan
GPF-plus [5]	104.54 ± 0.26	130.76 ± 1.28	104.51 ± 0.57	155.02 ± 0.51
GeoAda	91.03 ± 0.33	120.35 ± 0.44	76.94 ± 0.45	129.81 ± 0.30

9.3 Ablations

9.3.1 Parameter efficiency analysis

As shown in Table 20, we explore the impact of varying the number of equivariant adapter blocks. Increasing the number of trainable copy layers generally improves performance, but introduces more parameters and computational cost, revealing a trade-off between performance and efficiency. We have computed the number of tunable parameters for all baselines and GeoAda. The statistics are presented in Table 21. Except for Full Fine-Tuning, all methods have a comparable number of tunable parameters, ensuring a fair comparison.

Table 20: Different numbers of adapter blocks

Number	ADE	FDE
1	1.321	3.088
2	1.291	2.968
3	1.108	2.621
4	1.104	2.588
5	1.106	2.686

Table 21: The number of tunable parameters for different tuning strategies.

Dataset	Tuning Strategy	Total Parameters	Tunable Parameters
Charged Particle	Full FT	1418252 ~5.41 MB	1418252 ~5.41 MB
	PARTIAL- k	1418252 ~5.41 MB	711302 ~2.71 MB
	MLP- k	2125202 ~8.11 MB	711302 ~2.71 MB
	Prompt-Tem	1418252 ~5.41 MB	711302 ~2.71 MB
	GPF	2125266 ~8.11 MB	711366 ~2.71 MB
	GPF-plus	2125847 ~8.11 MB	711947 ~2.72 MB
	GeoAda	2125691 ~8.11 MB	711791 ~2.72 MB
MD17	Full FT	1424268 ~5.43 MB	1424268 ~5.43 MB
	PARTIAL- k	1424268 ~5.43 MB	716166 ~2.73 MB
	MLP- k	2132370 ~8.13 MB	716166 ~2.73 MB
	Prompt-Tem	1424268 ~5.43 MB	716166 ~2.73 MB
	GPF	2132434 ~8.13 MB	716230 ~2.73 MB
	GPF-plus	2135079 ~8.14 MB	718875 ~2.74 MB
	GeoAda	2132844 ~8.14 MB	716640 ~2.73 MB
CMU Mocap	Full FT	368012 ~1.40 MB	368012 ~1.40 MB
	PARTIAL- k	368012 ~1.40 MB	185990 ~0.71 MB
	MLP- k	550034 ~2.10 MB	185990 ~0.71 MB
	GPF	550098 ~2.10 MB	186054 ~0.71 MB
	GPF-plus	553259 ~2.11 MB	189215 ~0.72 MB
	GeoAda	550075 ~2.10 MB	186031 ~0.71 MB

9.3.2 Ablative Architectures

We study the following ablative architectures as shown in Figure 6, Figure 7, Figure 8:

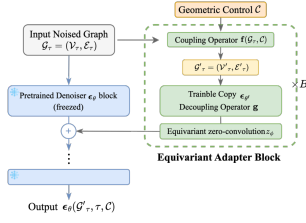


Figure 6: GeoAda

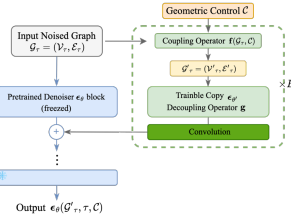


Figure 7: w/o zero convolution

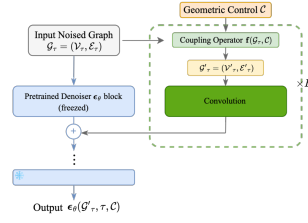


Figure 8: w/o trainable copy

Proposed GeoAda. The proposed architecture in the main paper.

Without Zero Convolution. Replacing the zero convolutions with standard convolution layers initialized with Gaussian weights.

Lightweight Layers. This architecture does not use a trainable copy, and directly initializes single convolution layers.

Results We present the results of this ablative study in Table 22, Table 23, Table 24 and Table 25.

Table 22: Comparisons for Molecular Dynamics prediction on MD17 dataset (all results reported by $\times 10^{-1}$). The best results are highlighted in bold. Results averaged over 5 runs

Scenarios	Aspirin				Benzene			
	FT		Pretrain		FT		Pretrain	
	ADE	FDE	ADE	FDE	ADE	FDE	ADE	FDE
w/o trainable copy	2.232 \pm 0.008	3.501 \pm 0.022	2.197 \pm 0.007	3.449 \pm 0.010	0.607 \pm 0.002	0.952 \pm 0.010	0.584 \pm 0.002	0.948 \pm 0.006
w/o zero conv	0.929 \pm 0.002	1.619 \pm 0.009	1.203 \pm 0.009	1.975 \pm 0.018	0.214 \pm 0.001	0.359 \pm 0.004	0.291 \pm 0.001	0.469 \pm 0.007
GeoAda	0.891 \pm 0.003	1.533 \pm 0.008	1.060 \pm 0.003	1.852 \pm 0.012	0.191 \pm 0.000	0.319 \pm 0.002	0.240 \pm 0.002	0.394 \pm 0.005

Table 23: Ablation study of Short-term prediction on **running** from the CMU Mocap dataset.

scenarios	running				pretrain			
millisecond (ms)	80	160	320	400	80	160	320	400
w/o trainable copy	44.52 \pm 0.48	76.98 \pm 1.20	134.91 \pm 2.04	159.75 \pm 2.45	198.16 \pm 2.97	139.24 \pm 0.23	270.04 \pm 0.56	314.89 \pm 0.68
w/o zero conv	19.07 \pm 0.37	34.25 \pm 0.82	51.75 \pm 1.39	55.74 \pm 1.53	nan	nan	nan	nan
GeoAda	18.70 \pm 0.37	33.56 \pm 0.25	50.26 \pm 0.42	55.54 \pm 0.36	7.972 \pm 0.02	16.91 \pm 0.05	40.06 \pm 0.42	52.61 \pm 0.07

Table 24: Ablation study of Short-term prediction on **walking** from the CMU Mocap dataset.

scenarios	walking				pretrain			
millisecond (ms)	80	160	320	400	80	160	320	400
w/o trainable copy	23.77 \pm 0.15	43.43 \pm 0.31	84.79 \pm 0.77	105.08 \pm 1.28	nan	nan	nan	nan
w/o zero conv	12.62 \pm 0.07	20.67 \pm 0.20	36.75 \pm 0.52	44.69 \pm 0.45	36.18 \pm 0.12	58.18 \pm 0.08	102.06 \pm 0.05	123.82 \pm 0.04
GeoAda	8.92 \pm 1.02	13.82 \pm 1.26	22.99 \pm 1.30	26.68 \pm 1.31	7.932 \pm 0.03	16.90 \pm 0.04	38.96 \pm 0.47	52.54 \pm 0.10

Table 25: Ablation study of long-term prediction on **running, walking** from the CMU Mocap dataset.

scenarios	running		pretrain		walking		pretrain	
millisecond (ms)	560	1000	560	1000	560	1000	560	1000
w/o trainable copy	198.16 \pm 2.97	228.41 \pm 2.96	365.41 \pm 0.63	374.74 \pm 0.48	143.35 \pm 2.26	214.78 \pm 2.82	nan	nan
w/o zero conv	64.69 \pm 0.97	74.64 \pm 0.66	nan	nan	60.28 \pm 1.07	93.99 \pm 1.41	165.86 \pm 0.15	249.90 \pm 0.38
GeoAda	60.88 \pm 0.82	70.22 \pm 2.02	77.22 \pm 0.45	130.17 \pm 0.26	34.52 \pm 2.26	50.49 \pm 0.33	78.12 \pm 0.49	129.97 \pm 0.30

9.4 Standard Deviations

We have already provided the standard deviations in App. 9.2.

10 Discussion

Limitation While GeoAda demonstrates strong empirical performance and theoretical grounding in preserving $SE(3)$ -equivariance during fine-tuning, several limitations remain: The effectiveness of GeoAda hinges on the design of coupling and decoupling operators for control injection. While theoretically sound, these handcrafted designs may not generalize well to control signals with high-dimensional or structured semantics. Moreover, although GeoAda is validated across multiple domains (e.g., particles, molecules, human motion), the evaluations are limited to medium-scale datasets and relatively small models. Assessing its scalability to larger systems—such as full proteins or macromolecular assemblies—remains an important direction for future work.